Flinders
UNIVERSITY

Mechanism of Organic Solar Cell Performance Degradation upon Thermal Annealing of MoO_x

Yanting Yin[1,2], Xun Pan[1], Mats R. Andersson[1], David A. Lewis[1] and Gunther G. Andersson*[1,2]

1 Flinders Institute for Nanoscale Science and Technology, Flinders University, Adelaide SA 5042, Australia

2 Flinders Microscopy and Microanalysis, College of Science and Engineering, Flinders University, Adelaide, SA 5042, Australia

** Gunther.Andersson@flinders.edu.au*

Abstract

In this work we focus on P3HT:$PC_{61}BM$ bulk heterojunction (BHJ) devices with MoO_3 at the hole extraction side of the BHJ which relies on the formation of a strong dipole at the BHJ/MoO_3 interface, as a reference system that has been extensively studied. We have observed depending on when the annealing is performed during device fabrication, device performance either increased or decreased due to formation of a sharp or relatively diffuse interface respectively due to diffusion of MoO_x into the BHJ. The measured strength of the dipole at this interface following thermal annealing correlated well with the width of the interface and device performance, with the sharper interface resulting in a stronger dipole and in improved device performance. This is expected to be a general phenomenon for evaporated coatings onto polymeric BHJ, regardless of the polymers involved.

Key words: Organic solar cell, MoO_3, Interface dipole, Thermal annealing, Energy level alignment

Introduction

The inverted type [1-2] of polymer-based solar cell consists of a sandwiched structure of substrate/cathode/cathode buffer layer (CBL)/polymer-fullerene (donor and acceptor)/anode buffer layer (ABL)/anode[3-4]. High workfunction (WF) transition metal oxides (TMOs) such as molybdenum trioxide (MoO_3), vanadium oxide (V_2O_5) and tungsten trioxide (WO_3) are used as the ABL to boost the charge transport efficiency [4-5] which has been ascribed to the charge transport at such interfaces through a charge injection/extraction mechanism, based on the alignment of the highest occupied molecular orbital (HOMO) of the organic layer and the conduction band (CB) of the TMOs[6 7 8]. The formation of diploes at the interface between the layers forming an organic electronic device can lead to the alignment of the energy levels at the interface[6, 9-10]. The position of the energy levels can be measured directly[6, 10] and can also be estimated from the WFs of the materials forming the interfaces[11-14].

Thermal treatments are used at various points throughout the fabrication of devices to remove solvents, develop morphology, such as following deposition of the BHJ [15-19], and complete cure chemistry or relieve thermal stress following the deposition of the TMO such as MoO_3 [2, 20] through the sol-gel method, laser deposition[21]. Thermal treatment of the BHJ exceeding the glass transition temperature (T_g) of conjugated polymers[22] results in a higher charge mobility [23-25] due to a reorganization of the materials in the polymer BHJ [15, 26-27]. Further benefits observed are the increase of polymer crystallinity [1, 15-16, 22] resulting in the enhancement of the optical response and charge mobility. Overall, it has been reported that the spectral response and the power conversion efficiency (PCE) of the devices can increase upon annealing on BHJ [1-2, 16, 26, 28].

Annealing of the devices after the deposition of the MoO_3 can have various effects, however.

Battaglia et. al have reported that annealing following MoO_3 deposition leads to the occurrence of intermediate energy states between the Fermi edge and valence band (VB) edge of the pristine MoO_3 due to the formation of oxygen vacancies, i.e. MoO_x defects [29]. It was found that MoO_x defect states could facilitate the transfer of holes over the BHJ/MoO_3 interface [30], which would be beneficial for the device performance. On the other hand, annealing of samples after the formation of the BHJ/MoO_3 interface causes diffusion of the MoO_3 into the BHJ layer.[2, 31] Greiner et al. also reported reduction of MoO_3 to MoO_x at 150 ^{o}C and a decrease of the MoO_3 WF by 1.1 eV [32]. It can be anticipated that the decrease of the MoO_3 WF by 1.1eV will induce a significant change of the dipole formation at the BHJ/MoO_3 interface. The reason for this assumption is that the decrease in the MoO_3 WF indicates a decrease of the polarity of the surface of MoO_3 upon annealing, which consequently should also decrease the polarity at an interface formed by the MoO_3 and thus the dipole strength at the BHJ/MoO_3 interface and thus also of the dipole at that interface. However, the change of the dipole at the surface of the MoO_3 is not necessarily the same as the change of the dipole at an interface formed by the MoO_3. A change of the dipole at the BHJ/MoO_3 interface might also affect the charge transport over the interface as outlined above and thus the device performance.

The aim of the present work is to determine how the annealing conditions of the BHJ/MoO_3 interface influence the concentration depth profiles of the components across the interface, in particular the concentration depth profiles of Mo, the chemical state of the MoO_3 and the valence electron structure of the interface. The diffusion of MoO_3 into polymers is known[2] as well as the formation of a strong dipole at the BHJ/MoO_3 interface[6]. The results demonstrate that MoO_3 diffuses into the polymer, thereby decreasing the dipole formed at the BHJ/MoO_3 interface and causing the decrease in device performance. The analysis of the composition, the chemical state of the MoO_3 and the valence electron structure is correlated to the performance of organic photovoltaic (OPV) devices.

This correlation between the shape of the concentration depth profile across the interface and dipole strength is likely to occur for many combinations of metal oxide/BHJ interfaces used in organic electronic devices.

Experimental

X-ray Photoelectron Spectroscopy (XPS) has been applied to investigate the elemental composition and the chemical states of the elements forming the samples [33-34] using Mg Kα radiation. The probing depth is a few nm and depends on the kinetic energy of the electrons emitted from a specific element. The ultra-high vacuum (UHV) apparatus was built by SPECS (Berlin, Germany) with a non-monochromatic X-ray source. The angle between the irradiation and spectrometer is 54°. Survey spectra have been recorded at a pass energy of 40 eV. High resolution spectra of Carbon, Oxygen, Molybdenum and Sulfur have been determined at a pass energy of 10 eV. We usually calibrate the XPS binding energy scale by normalizing the C1s peak related to C-C at 285 eV. However, as shown in our earlier work on the MoO_3/BHJ interface a dipole can form at the interface causing a shift of some of the C1s components in the spectra. As a consequence the usual energy calibration procedure cannot be applied to the XP spectra of the MoO_3/BHJ interface and hence calibration of the energy scale was not applied. [6] There was no evidence of charging.

Ultra-violet Photoelectron Spectroscopy (UPS) have been used to determine the workfunction (WF) [35-36] and measuring valence electron spectra at a pass energy of 10 eV. A two-stage cold cathode discharge is used to generate HeI UV radiation and metastable He atoms (He*) simultaneously. Samples have been biased by -10 V when collecting UP spectra. The UPS is sensitive up to a depth of 2.5~3 nm with an excitation energy of 21.2 eV. The valence electron spectra derived from UPS have been analyzed applying the singular value

decomposition algorithm as described in detail previously [6, 37-38].

Neutral Impact Collision Ion Scattering Spectroscopy (NICISS) is used to determine concentration depth profiles of the elements with a few Å depth resolution.[39] The probing depth in a soft-matter surface is around 30 nm [40]. In a NICISS experiment a pulsed beam of He ions with a kinetic energy of a few keV is directed onto a sample surface. The He projectiles lose energy when being backscattered from the atoms forming the sample. The energy loss due to backscattering depends on the atomic mass of the projectile and the target atom. By measuring the time of flight (TOF) of the backscattered projectiles the energy loss of the projectiles is determined. The Helium projectiles also lose energy on their trajectory through the bulk of the sample through small-angle-scattering and electronic excitations (stopping power). This second type of energy loss is proportional to the depth from which the projectile is backscattered and allows for determining the concentration depth profiles of the elements forming the samples[41]. The maximum dose of the ion beam on a given spot of the sample is kept below $5 \cdot 10^{13}$ ions/cm^2 in order to avoid measurable change of the sample composition due to damage by the ion beam. It needs to be noted that the energy loss of He^+ in MoO_3 has not yet been determined. The uncertainty of correlating the energy loss to the depth scale is thus larger than that reported for other experiments [42] but still sufficient for the present work. For this reason, both energy loss scale and the depth are shown as x-axis.

Inverse Photoelectron Spectroscopy (IPES)[7-8] allows probing the electronic structure of the unoccupied states. The technique directs electrons emitted from a BaO filament onto a sample which enter into the unoccupied states of the samples which have an energy difference to the Fermi level which is less than their kinetic energy resulting in the emission of photons. The difference in kinetic energy of the electrons and the energy level of the entered occupied state determines the energy of the emitted photon. A photon detector using a mixture of Ar and acetone has been used. The emitted photons are detected as a function of the kinetic energy of

the electrons and allow measuring the IPE spectrum. By operating insitu-IPES subsequent to UPS, a complete energy band structure of sample is acquired.

The device fabrication and the J-V characterization are further described in the supporting information.

Data evaluation of UPS and IPES

Characterizing the workfunction (WF), energy position of valence band (E_{VB}) /highest occupied molecular orbital (E_{HOMO}) and conduction band (E_{CB})/lowest unoccupied molecular orbital (E_{LUMO}): As has been shown in a previous publication[6, 43], deconvolution of the secondary electron cut-off with a Gaussian function representing the energy resolution of the experiment can be applied for determining accurately the WF. The E_{HOMO} and E_{VB} can be determined from valence electron region of UPS. The base line and the valence electron cut-off are both plotted with linear functions and their intersection is taken as E_{HOMO}. The same procedure has been applied to the conduction band region in the IPE spectrum, which is used to determine the E_{LUMO} and E_{CB}. The E_{VB}/E_{HOMO} and E_{CB}/E_{LUMO} in this work represent the energy difference between E_{VB}/E_{HOMO} and the Fermi level and E_{CB}/E_{LUMO} and the Fermi level, which both are absolute measures.

Analysis of the UP spectra: Singular Value Decomposition (SVD) [37, 44-45] has been used for analyzing UP spectra and for identifying the components which comprise the measured spectrum in same way as our previous work[6]. UP spectra of a sample consisting of more than a single component can be described as linear combination of the UP spectra of the individual components. The purpose of applying the SVD algorithm is to identify the spectra of the individual components and to determine the contribution of the spectra of the individual components to the UP spectrum of a specific sample. For applying the SVD algorithm a series of spectra prepared by changing a single or very few parameters but otherwise same conditions

has to be measured. It should be noted that it is in the nature of SVD that the reference spectra resulting from the applying the algorithm are not necessarily entirely identical with the spectra of a surface formed by a specific substance. The reason is that the SVD algorithm can lead to a small degree of intermixing of the spectra of the plain substance or adding or removing the secondary electron background.

Sample Preparation

P3HT (Poly(3-hexylthiophene-2,5-diyl) of 99.9% purity from Rieke Metals (U.S.) and $PC_{61}BM$ ([6,6]-Phenyl C61 butyric acid methyl ester) of 99.9% purity from Solenne Bv (Netherlands) were solved in 1,2-dichlorobenzene(*o*-DCB):chlorobenzene (30:70 wt%). The material concentration in solutions was 3 wt% [46]. After being stirred for 10 hours at 60 °C, the solution was spin-coated at 2200 rpm for 60 s on low-resistance As-doped Si wafers in a glove box with N_2 atmosphere. The samples were then heated at 80 °C for 10 min to ensure complete solvent removal. All samples were prepared from the same batch of organic materials. The temperature for annealing was ramped and held at 170 °C for 10 min. The annealing temperature was selected according to previous works [15-16]. Samples were annealed under UHV conditions. Subsequently XPS, UPS and NICISS were applied in the same UHV chamber, i.e. without exposing the samples to ambient conditions between annealing and surface characterization.

MoO_3 with a purity of 99.95% from S-Aldrich was evaporated at 535 ºC under high vacuum ($<10^{-6}$ mbar). The deposition rate was set to 0.02 nm/s and measured with a quartz crystal microbalance and a thickness of 1.5 nm on BHJ was achieved. Samples were transferred to analysis chamber for applying ion scattering and electron spectroscopy without exposure of the samples to air. The fabrication process for four different types of samples are described in Table 1 and illustrated in Figure 1.

Table 1. Samples as a structure of evaporating MoO_3 on P3HT:$PC_{61}BM$ BHJ, the thermal annealing was performed at different stage at 170 ºC for 10 min (√: annealing processed, otherwise not)

Number	*Sample name*	*Process 1*	*Thermal annealing*	*Process 2*	*Thermal annealing*
1	Non-annealed	P3HT:$PC_{61}BM$ film coated		MoO_3 evaporated	
2	Pre-annealed		√		
3	Post-annealed				√
4	2-stage annealed		√		√

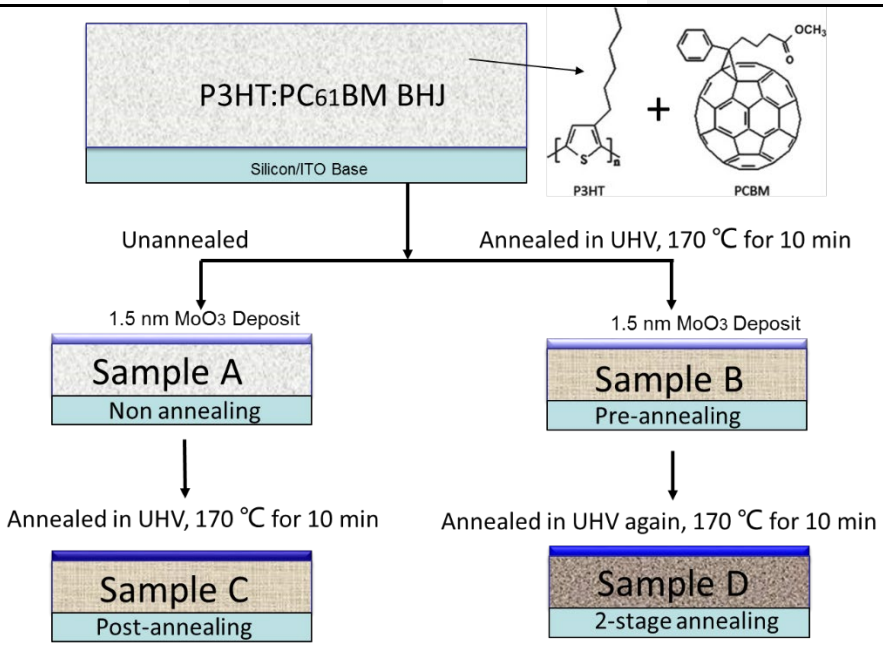

Figure 1. MoO_3/P3HT:$PC_{61}BM$ sample preparation, the process for performing of the annealing is shown

Further, a sample with 4 nm MoO_3 deposited onto the BHJ was also fabricated as a reference for the depth profiling measurements.

In order to evaluate the performance of polymer-based solar cell performance with four different annealing conditions, solar cell devices with the respective annealing process have been fabricated and characterized. The fabrication details of solar cells based on P3HT:PCBM is provided in the supporting information. It should be noted that the structure of the solar cells

was not optimized for highest performance.

Results

Elemental Concentration Depth Profiles at the MoO_3/BHJ Interface upon Annealing

The Mo concentration depth profiles as measured with NICISS in Figure 2 show that upon evaporation of 1.5 nm of MoO_3 on a non-annealed polymer sample, the Mo penetrates up to 10 to 15 nm into the polymer layer with an asymmetric profile with a long tail towards larger depth. The maximum of the Mo concentration for the non-annealed sample is found at approximately 2 - 3 nm. Previous research had shown that a deposition of approx. 1.0 nm is required to achieve closed surface coverage on pre-annealed P3HT:PCBM [6].

The maximum concentration of the Mo concentration depth profile of the pre-annealed sample is found around 0.5 - 1 nm depth with a similar slope towards larger depth as the non-annealed sample, indicating that the Mo penetrates into the pre-annealed sample to a slightly lesser degree than for the non-annealed sample.

The maxima of the Mo concentration of the post-annealed and the two-stage annealed sample is found to be 5 – 6 nm and thus at a significant larger depth than for the samples that had not been annealed after the MoO_3 deposition. It can be concluded that annealing after the deposition of MoO_3 causes diffusion of the Mo into the BHJ, or of the P3HT towards the air / vacuum surface

Importantly, the Mo concentration depth profiles for 4nm layers of MoO_3 that are more likely to be used in device fabrication, are similar to those of the 1.5 nm MoO_3 layers, as seen in Figure S6. It should be noted that the concentration depth profile of the non-annealed sample is slightly different to the concentration depth profile of the previous published profile[6]. The reason is probably some differences in the preparation of the BHJ layer.

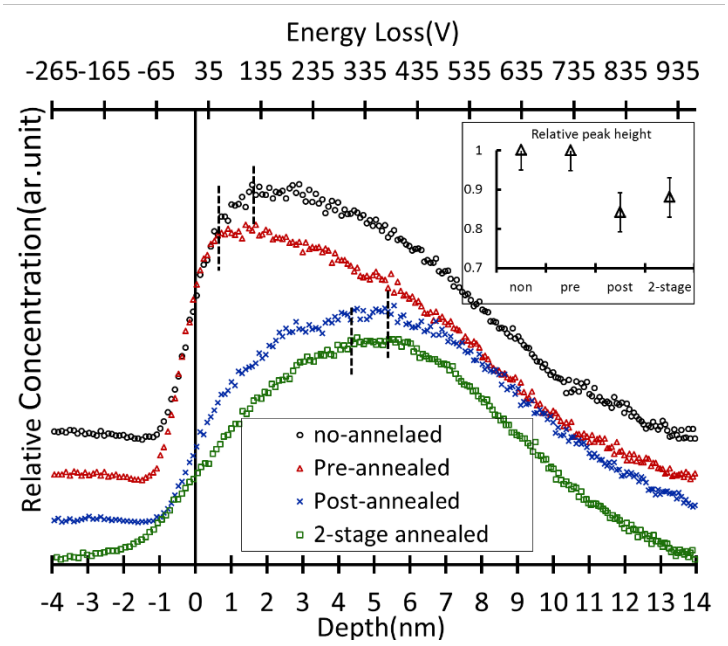

Figure 2. The depth profile of Mo derived from NICISS under different conditions of annealing, the inset illustrates relative peak height

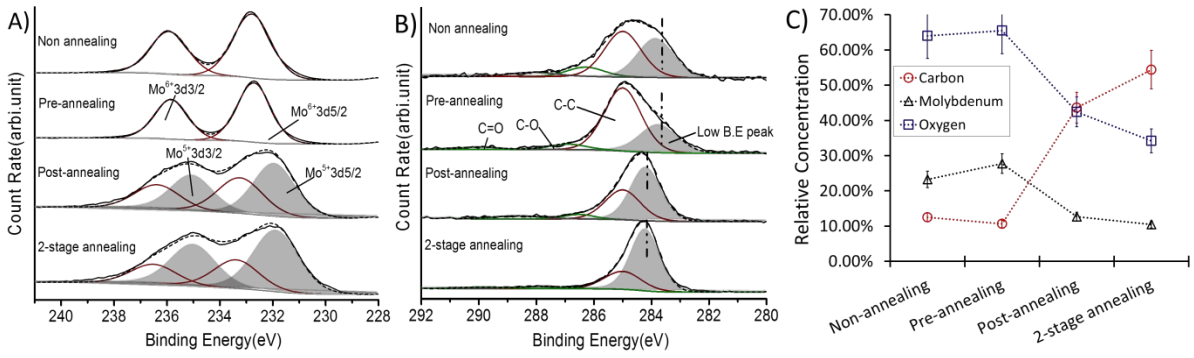

Figure 3. A), B) fitting of the Mo and C spectra of XPS, the Mo^{5+} contribution is marked with a shading; C) the relative concentration of C, Mo and O as a function of annealing conditions, the error bar of the peak position is ±0.15 eV while the relative concentration have an uncertainty of ±10%

In Figure 3 (A) and (B), high resolution XP spectra of Mo $3d_{5/2}$ and C1s are shown including fitting of the spectra. Relative concentrations of Mo, C and O can be seen in Figure 3 (C). The spectra of O and S are provided in Figure S1. A pristine BHJ sample (not shown here) was

measured before and after annealing under the same condition. Annealing did not noticeably change the spectrum of the BHJ.

The $Mo3d_{5/2}$ peak was found at 233.0 eV[24, 47] for the non- and pre-annealed samples. Post-annealed samples showed two $Mo3d_{5/2}$ contributions at positions of 233.1 eV and 231.7 eV[48]. The change in binding energy corresponds to the reduction of Mo in MoO_3 from Mo^{6+} to Mo^{5+}. The concentration of Mo^{5+} after annealing is in the range of 60%~70%. A similar phenomenon has been reported in reports elsewhere [30, 32]. Ahmadpour et. al. found that the reduction of MoO_3 due to annealing depends on the deposition method of the MoO_3 layer. In the fitting of the C peak four individual components can be identified: C-C sp2, C-O and C=O/C=O-H peaks are found at 285.0 eV, 286.7 eV and 288.0 eV [49-50]. The C peaks at low binding energy ranging from 283.7 eV to 284.2 eV have been discussed in our previous work[6] and are due to the formation of a dipole at the MoO_3/BHJ interface. The fraction of C found at binding energies < 285 eV in the non-annealed and pre-annealed samples is less than in the post-annealed and 2-stage annealed samples. However, the position of the C peak of the contribution at < 285 of non-annealed and pre-annealed samples is lower by about 0.5 eV compared to the post-annealed and 2-stage annealed samples. The reason for this are differences in the strength of the dipole at the MoO_3/BHJ interface which will be discussed below.

Figure 3 (C) shows that the relative concentration of C is increased dramatically from about 10% for the non-annealed and pre-annealed sample to 50% for the post-annealed and 2-stage annealed sample with the amount of O and Mo decreasing. This finding reflects the diffusion of Mo into the BHJ due to the post-annealing as found in the concertation depth profiles determined with NICISS. The overall concentration of Mo in the near surface region after deposition of the MoO_3 is the same for all samples. However, the intensity of the XPS signal is attenuated exponentially with depth. Thus, the XPS intensity of Mo decreases in the case that Mo moves to a deeper layer with thermal annealing.

Analysis of Electrical Properties of MoO_3/BHJ Interface upon Annealing

a) Analysis of UPS of the MoO_3/BHJ Interface for all Annealing Processes

The secondary electron cut-off for the samples and the valence electron region derived from UPS are shown in Figure 4 (A) and (B). The WF is shown in Figure 4 (C). A pristine sample of BHJ and a sample of 8 nm MoO_3 on Si were processed under the same annealing conditions and the combined result of UPS and IPES is included in Figure S2 and Figure S3.

Neither the secondary electron cut-off nor the valence electron spectra of BHJ changes after annealing of the plain BHJ sample, indicating no energy level structure of BHJ has been altered.

In contrast, the WF of MoO_3 on Si decreases from 6.8 eV to around 4.8 eV and new states are found in the band gap. The states in the band gap are from partially reduced MoO_3 (MoO_x ,x~2.5) contributing to a higher conductivity as has been shown in references [32, 34, 51]. Ahmadpour et. al. have shown that device efficiency improves after annealing at 200 ^{o}C of sputter deposited MoO_3 without formation of reduced MoO_3 which implies that increasing conductivity due to the annealing is not necessary for improving the efficiency.[52] No significant change of the onset of the IPE spectrum of the WF of MoO_3 sample can be seen, indicating that the E_{CB} of both pristine MoO_3 and annealed MoO_x stay constant at 0.4eV. The band gap (E_g) of MoO_3 was determined from evaluating UPS and IPES measurements by extracting the valence and conduction peaks cut-off, as shown in Figure S3, which decreases from 3.0 eV to 1.4 eV ($\pm$0.2).

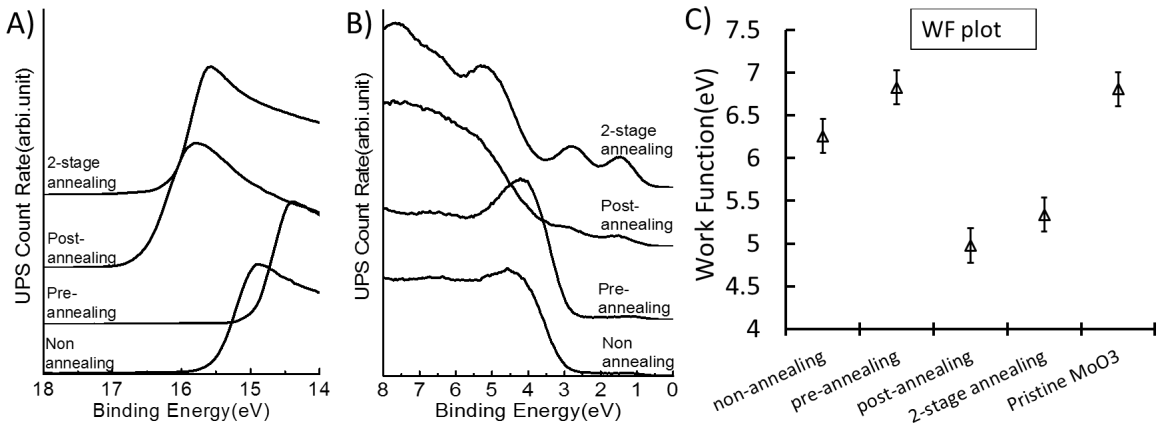

Figure 4. (A) Secondary electron cut-off of UP spectra; (B) Valence electron region of UP spectra; (C) WF plot of the samples; The error bar for WF, $E_{VB/HOMO}$ and $E_{CB/LUMO}$ are ±0.1 eV

As can be seen in Figure 4 (A), the secondary electron cut-off or WF after deposition of MoO_3 changes significantly, depending on the thermal treatment. After deposition of MoO_3, the WF of the pre-annealed sample is 6.8 ± 0.1 eV, which is close to the WF of pristine MoO_3 [14]. From NICISS measurements, this sample also showed the highest surface concentration of Mo of all of the samples examined.

The WF for the non-annealed sample is reduced to 6.4 ± 0.1 eV and following post-MoO_3 deposition annealing, the WF decreases further to 4.8 ± 0.1 eV and 5.3 ± 0.1 eV.

In the valence electron region shown in Figure 4 (B), peaks at around 1.8 eV and 2.8 eV have formed in the post- and 2-stage annealed samples. The spectrum of the annealed MoO_3/BHJ sample in Figure 4 (B) shows features which are different to those in the spectrum of the annealed MoO_3/Si sample in Figure S3. The change in the MoO_3/BHJ valence electron region at the interface is complex and requires a separate analysis procedure which will be shown and discussed below.

b) Decomposition of valence electron region of UPS

SVD has been applied on the valence electron region of the UP spectra of the non-annealing,

pre- and post-annealing and 2-stage annealing samples to identify the components constituting the measured spectra. The reference spectra representing the constituting components and the corresponding weighing factors are shown in Figure 5 (A). Figure 5 (B) and (C) are used to identify the nature of the reference spectra. The fitting of the spectra is shown in Figure S4.

The purpose of the detailed analysis of the UP spectra is to identify how and why the electronic structure of the MoO_3/BHJ surface is changing due to the annealing procedure.

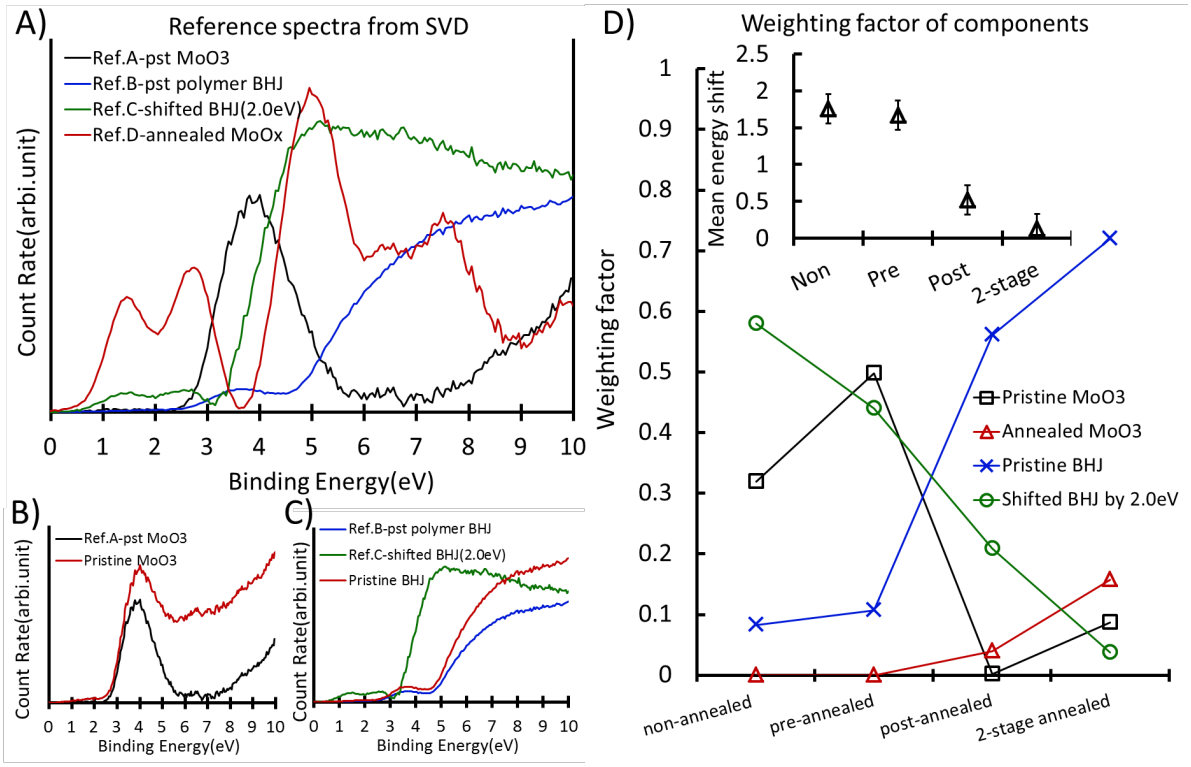

Figure 5. A) The UP reference spectra identified applying SVD; B) and C) comparison of the reference spectra with a pristine MoO_3 and a BHJ spectrum; D) The weighting factor of reference spectra, the inset shows the calculated mean energy shift as calculated with the procedure described in reference[6] and the supporting information. The mean energy shift represents the strength of the dipole formed at the MoO_3/BHJ interface.

Figure 5 (A) shows the four reference spectra required to fit the whole set of the four measured spectra. Ref. A has features very similar to those of the spectrum of pristine MoO_3 and thus is

assigned to pristine MoO_3. The peak at 4eV is characteristic for MoO_3 [11].

As shown in Figure 5 (C), Ref. B can clearly be attributed to the pristine BHJ. Ref. C is very similar in shape to Ref. B but is subject to a shift to lower binding energy region by around 2.0 eV. Such a reference spectrum had been identified in our earlier work[6] and represents the BHJ being subject to a shift on the energy scale due to the formation of a strong dipole between the BHJ and MoO_3. Ref. C also seems to show to a small degree a contribution from Ref. D. The reason of a small proportion of mixing of spectra has been described in the Experimental section.

Ref. D has several characteristic peaks, namely at 1.5 eV, 2.6 eV, 5 eV and 7.6 eV. The peaks at 1.5 eV and 2.6 eV are in the gap between HOMO and LUMO of the BHJ and the band gap of MoO_3 and change the semiconducting nature of both MoO_3 and the BHJ. They can lead to enhanced charge transport but also act as recombination sites for electrons and holes or as trap states for either charge carrier[53-54]. The exact nature of the substance represented by Ref. D is not entirely clear. It could be reduced MoO_x with oxygen vacancies and Mo at lower oxidation states than 6, but it could also be a mixture of MoO_x and polymer BHJ.

The weighting factors of the four reference spectra for fitting the measured spectra are shown in Figure 5 (D). The non-annealed sample and the annealed sample show mainly contributions of MoO_3 and the shifted BHJ spectrum, which is consistent with previous reports for the deposition of MoO_3 onto the BHJ. [6] The post-annealed sample shows a decrease of the shifted BHJ spectrum and a very strong contribution of the pristine BHJ spectrum, while the contribution of the pristine MoO_3 has disappeared. Also, no significant contribution of the MoO_3 in the post-annealed sample is found. This finding is consistent with NICISS and XPS results, which had shown that the MoO_3 moves to deeper layers when the samples are annealed. A similar trend can also be seen for the two stage annealed sample, however, a significant presence of MoO_3 at the surface remains.

While the change in WF due to annealing could to some degree be due to the change in chemical state (reduction) as indicated by XPS, the magnitude of the decrease in concentration of the MoO3 at the surface suggests that it is more likely due to the formation of a mixture of MoO_3 and BHJ forming at the surface. It should be noted that the WF has been shown to depend on the substrate as described by Bao et al.[55] but in the present case this will probably not be a major contribution to the change in WF because the substrate is the same for all samples.

The dipole at the BHJ/MoO_3 can be calculated with the procedure described[6] and summarized in the supporting information section and is shown in Figure 5 (D). In contrast, a large fraction of BHJ with only a small energy shift was found for the post-annealing samples. As a consequence, the interface dipole of this sample is rather small. It is important to note that the energy shift found here is due to the formation of a dipole at the interface and not a difference in energy levels between the respective materials.

A second decomposition method as reported in [6] has also been applied to the UP spectra. The ΔE_{mean} found using the second procedure is in agreement with the results found through applying the SVD. The details are included in supporting information as shown in Figure S5.

Model for the Interface Dipole Formation and Consequence for the Charge Transport

Diagram for Composition and Dipole Formation at the Interface upon Annealing

Figure 6 shows a model for the MoO_3/BHJ interface region that accounts for the combined results from the valence electron structure derived from UPS, the chemical analysis with XPS and the concentration depth profiles of the elements measured with NICISS.

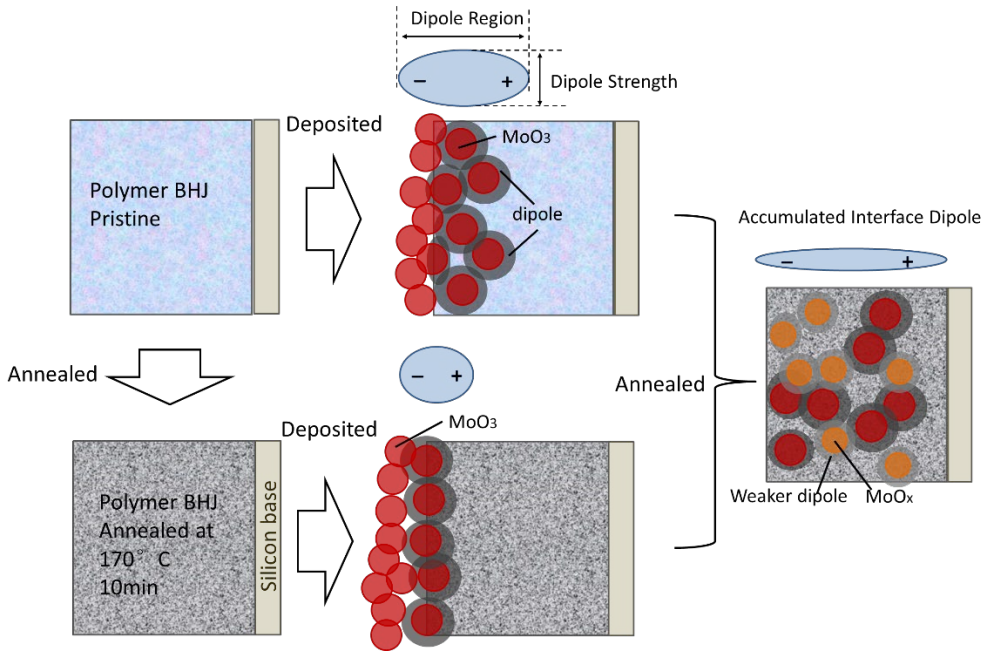

Figure 6. Illustration of the MoO_3/BHJ interface after annealing of the BHJ layer and before annealing. At the very right the interfaces of both the non-pre- and the pre-annealing are sketched that result in a similar distribution of the MoO_3.

The distribution of MoO_3 in the BHJ as function of the depth has been analyzed with NICISS. After annealing the MoO_3 has diffused to a larger depth. The reason for the diffusion is most likely that the surface energy of MoO_3 is larger than that of the polymer[56] , driving the MoO_3 particles to larger depth when the mobility [57]of the polymer and the MoO_3 increases at elevated temperatures [56, 58]. XPS result shows that the MoO_3 reduced at the applied temperature. The WF of the samples decreases upon annealing due to both the decrease in the concentration of MoO_3 at the surface and the reduction of MoO_3 to MoO_x. Compared to the non-reduced MoO_3, the MoO_x has a lower intrinsic WF.

The results can be summarised as:

i) Non-annealing after deposition of MoO_3 leads to a distribution of the MoO_3 into the BHJ and formation of a surface which shows both BHJ and MoO_3 at the surface and the formation of a strong dipole at the BHJ/MoO_3 interface in the order of 1.7 eV and

comparable with former results[6].

ii) Annealing of the BHJ before the deposition of the MoO_3 gives a well-defined interface.

iii) Annealing only after the deposition of MoO_3 removes almost all MoO_3 from the BHJ/MoO_3 surface and shows little formation of a dipole at the BHJ/MoO_3 interface. One of the reasons is that the MoO_3 is not present to a significant fraction in the outermost layer, which is more spread out over a greater depth. In the case, the dipole orientation between the MoO_x and the BHJ is distributed in all directions due to the increase in the number of isolated MoO_x particles. The individual dipoles are less likely to accumulate to form an interface dipole, which points as vector from BHJ towards the side of MoO_3[6].

iv) Annealing before and after deposition of MoO_3 results in a surface which is composed of mostly BHJ and a small amount of MoO_3 and shows little formation of a dipole at the BHJ/MoO_3 interface. Only a small fraction of the MoO_3 is present in the outermost layer. The structure of this sample is rather similar to the sample with the post-annealed interface.

v) From post annealed and two-stage annealed samples, the reduction of MoO_3 and formation of MoO_x also produces a reduced WF. The dipole strength is further decreased because an interface dipole strongly depends on the difference of WF of the adjacent materials[9, 59-60].

Estimation of Charge Transport over the Interface upon Various Annealing Treatments

Figure 7 shows the energy level diagram based on the electron spectroscopy data and SVD analysis of the MoO_3/BHJ interface, illustrating the energy levels and their relative positions and also indicates the implication for the charge transport over the interface after applying annealing at the various conditions investigated here. The energy levels Fermi level (E_f), E_{CB} or E_{LUMO}, E_{VB} or E_{HOMO} are taken from the electron spectroscopy measurements directly or

from the analysis of the spectra based on the SVD analysis. The value for ΔE_{mean} is from Figure 5 (D) and is representing the strength of the dipole formed at the interface. The left and right sides are representing the region of MoO_3 and BHJ, respectively. The middle region is the interface with the mixed BHJ/MoO_3 phase formed. In the mixed region, the dash lines are representing the energy levels of the BHJ and their shift on the energy scale. The values for MoO_3, annealed MoO_x and BHJ are shown in Table 2. The CB of annealed MoO_x is rather close to E_f.

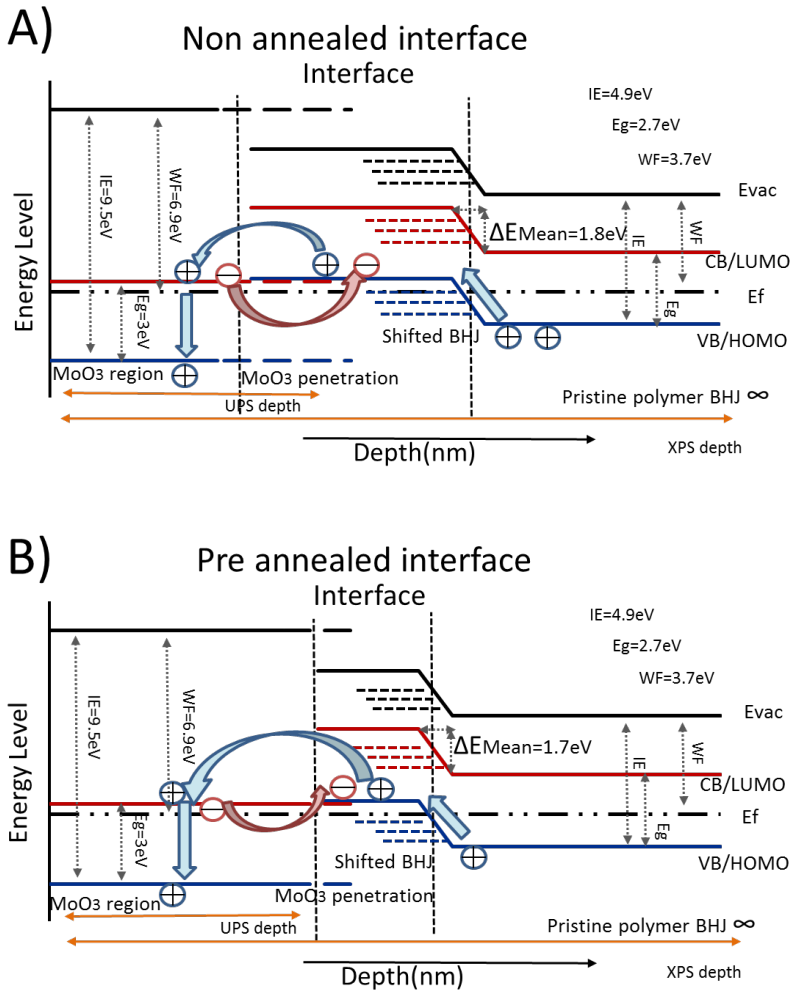

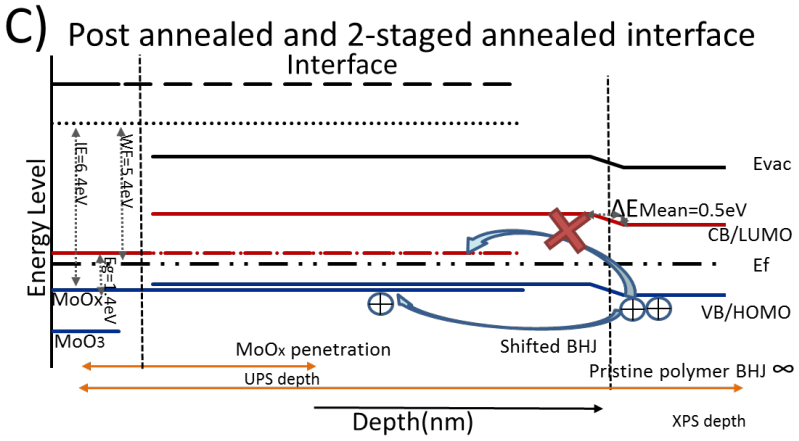

Figure 7. The energy level diagram of an interface with various annealing treatments, the assumed charge transport is included. In the non-annealed (A), pre-annealed sample (B) and post-annealed/2-stage annealed samples (C) intermediate energy states are formed at the MoO_3/BHJ interface as described in [6].

Table 2. Energy band parameters for BHJ and MoO_3 with/without annealing, it is important to note that the values of E_{CB}, E_{VB}, E_{LUMO}, E_{HOMO} shown here indicate the energy diversity from Fermi Level, with an error bar of ± 0.15 eV. Thus the absolute values are taken. EA-electron affinity; IE-ionization energy

Sample	***WF(eV)***	***E_{HOMO}/ E_{VB} (eV)***	***E_{LUMO}/ E_{CB} (eV)***	***E_g (eV)***	***EA(eV)***	***IE(eV)***
P3HT	3.6	1.1	1.6	2.7	2.0	4,7
$PC_{61}BM$	3.9	1.6	1.0	2.6	2.9	5.5
P3HT/$PC_{61}BM$ BHJ	3.7	1.2	1.5	2.7	2.2	4.9
MoO_3	6.8	2.6	0.4	3.0	6.4	9.4
Annealed MoO_x	4.8	1.2	0.4	1.4	4.4	6.0

In Figure 7 (A) the charge transport over the non-annealed MoO_3/BHJ interface follows the

mechanism as described elsewhere [6-8, 14] because the position of the energy levels of the BHJ have been shifted upwards at the interface due to the formation of the dipole at the interface. Thus the charge transport is facilitated through the formation of the dipole between the MoO_3 and the BHJ resulting in the HOMO of the BHJ positioned on the energy scale above the CB of MoO_3. This finding is in line with the work of Greiner et al. [11], Meyer et al. [14] and Ley et al. [12] who have estimated the alignment of energy levels. The energy level positions do not change significantly upon pre-annealing as shown in Figure 7 (B). The ΔE_{mean} levels at 1.7 eV and is sufficient for charge transport.

In contrast, for the post-annealed and 2-stage annealed sample in Figure 7 (C), ΔE_{mean} is 0.2 to 0.5 eV, which is not sufficient for an effective charge transport across the MoO_3/BHJ interface. The dipole formed is too small to shift the CB of MoO_3 above the HOMO of the BHJ and the energy levels do not match. Therefore, the extraction/injection is not as efficient as for the non-annealed and pre-annealed samples. It thus is expected that the efficiency of a solar cell fabricated with post annealing and with 2-stage annealing is lower than that of the non-annealed and the pre-annealed sample. The 2-stage annealed sample has the lowest dipole at the top electrode interface and is thus expected to have the lowest efficiency.

In the fabrication of a polymer-based photovoltaic device such as a solar cell using MoO_3 as a hole transport layer, the annealing process needs to be considered carefully. The pre-annealing of BHJ hindering the diffusion of MoO_3 particles into deeper depth in the BHJ is expected to be beneficial for achieving a favorable shunt resistance (R_{sh}). Further, the enhancement of light absorption of BHJ due to the pre-annealing could enhance the cell performance as reported [26] and the morphology and crystallinity have also been improved[16]. The post-annealing, however, is based on the above results expected not to be beneficial for the solar cell performance. The mismatch of the energy levels causes an energy barrier for charge transfer over the adjacent

interface and thus decrease in the efficiency. In order to verify the hypothesis that the post-annealing decreases the solar cell performance due to a mismatch in the energy level alignment, we have fabricated and characterized solar cells accordingly.

Solar Cell Device Performance with Various Annealing Conditions

The fabrication of the solar cell devices, glass/ITO/ZnO/P3HT:$PC_{61}BM$/MoO_3/Ag, is described in the supporting information. The devices have been treated after the deposition of the MoO_3 in the same way as the samples to which electron and ion scattering spectroscopy has been applied: non-annealed, pre-annealing of the BHJ before the deposition of the MoO_3, post-annealing after the deposition of the MoO_3 and two stage annealing. The J-V curve of the solar cells, the dark J-V characteristics and the resistance differential curve are shown in Figure S6 and the device characteristics for all six solar cells of each batch in Table S1. The averaged characteristics of the cells are listed in Table 3.

Table 3. Device characteristics of glass/ITO/ZnO/P3HT:$PC_{61}BM$/MoO_3/Ag based organic solar cells with different annealing process (averaged values with standard deviations in parentheses). R_s and R_{sh} were extrapolated from the dark J-V resistance differential in Figure S6. The structure of the solar cells was not optimised for highest performance.

Annealing condition	**PCE (%)**	***Voc* (V)**	***Jsc* (mA/cm²)**	**FF (%)**	***Rs* (Ω.cm²)**	***Rsh* (Ω)**
Non-annealed sample	2.85 (±0.05)	0.63 (±0.01)	10.02 (±0.12)	45.11 (±0.58)	1.40 (±0.01)	1124 (±4.75)
Pre-annealing of BHJ before MoO_3 deposition	3.71 (±0.03)	0.63 (±0.01)	11.45 (±0.31)	52.06 (±1.04)	1.24 (±0.01)	1147 (±4.92)

Post-annealing after MoO_3 deposition	0.90 (±0.03)	0.35 (±0.01)	6.41 (±0.16)	39.67 (±0.24)	1.53 (±0.02)	314 (±4.85)
2-stage annealing (before and after MoO_3 deposition)	0.12 (±0.01)	0.14 (±0.01)	4.76 (± 0.10)	30.50 (±0.25)	1.47 (±0.02)	190 (±5.22)

The solar cells with the pre-annealed BHJ have the highest PCE peaking at 3.71% and are about 20% higher than that of the non-annealed solar cells (2.85%) which has also been found by Chambon et al. [2]. The PCE of the post-annealed and the two-stage annealed solar cells are much lower: 0.90% and 0.12%, respectively. The decrease in PCE with post-annealing is due to a degradation in the electronic parameters- the open circuit voltage (V_{OC}); the short circuit current (J_{SC}) and fill factor.

It was found above that the MoO_3 diffuses into the BHJ during the post-annealing process which also changes the position of the energy levels at the BHJ/MoO_3 interface. Based on the energy level diagram shown in Figure 7, post-annealing causes a misalignment of the energy levels between the MoO_3 and the BHJ due to the decrease in dipole across the BHJ/MoO_3 interface and thus affects the charge injection/extraction transport [14], resulting in an increase of the serial resistance (R_s) and decreased V_{oc}. The penetration of MoO_3 into BHJ additionally deteriorates the R_{sh}. The characterisation of the solar cells with the respective treatment of the BHJ/MoO_3 interface provides evidence that the misalignment of the energy levels and penetration of MoO_3, and as a consequence affects the performance of the solar cells. The change in dipole at the BHJ/MoO3 interface is the dominant effect and correlates strongly with the device performance.

The penetration of the MoO_3 into the BHJ could also lead to doping of the BHJ and as a consequence also influence device performance. However, given that through the SVD analysis

only spectra with features of MoO_3 and BHJ have been found and no new component, we assume that this effect is minor. Meanwhile, a strong dipole is retained with a sharp interface due to pre-annealing of BHJ, improving the charge transport over the interface. Pre-annealing also has a positive influence upon BHJ as described in the introduction. Both facts lead to an improvement of the solar cell performance. Given that, the polymer solar cell using MoO_3 as anode buffer layer does not necessarily rely on MoO_x defect state for charge transport[29, 61], but a strong dipole at the interface can be beneficial.

It should be noted that the results found here most likely apply in a similar way to a large range of materials used for the active layer in polymer based solar cells.

Conclusion

Annealing has been applied at different stages of the deposition of MoO_3 onto a P3HT:$PC_{61}BM$ BHJ solar cell. It was found that depending on when the annealing process was carried out, that it i) influenced the chemical states of MoO_x, ii) affects the distribution of MoO_x along the depth scale iii) can decrease the dipole at the BHJ/MoO_3 interface and therefore decreases the charge transport over the interface and iv) can either significantly increase or decrease the efficiency of the device. The change in dipole at the BHJ/MoO_3 interface is the dominant effect and correlates strongly with the device performance.

Concentration profiles, measurements of the dipole strength demonstrate that if the P3HT in the BHJ is amorphous before the MoOx is deposited, thermal annealing promotes the diffusion of MoO_3 away from the BHJ/MoO_3 interface to deeper within the BHJ, which reduces the dipole strength and the device performance. This is the reason and mechanism for the reduced device performance of the post-annealed and 2-stage annealed devices. It is important to note that the P3HT based BHJ investigated in this paper is highly crystalline after annealing, and

results show that if the MoOx is deposited after initial thermal annealing, depth of penetration of MoO_3 in the annealed samples is significantly reduced, dipole strength maintained and device performance improved.

The implication is that other amorphous polymer based BHJ will show a similar depth of penetration as the non-annealed P3HT BHJ. It should be noted that depositing another layer on top of the MoO_3/BHJ could also change the distribution of components across the interface and influence the electronic structure of the interface. Also using lower annealing temperatures will lead to a less pronounced effect.

The decrease of the charge transport over the BHJ/MoO_3 interface affects both the V_{OC} and J_{SC} and results in a strong decrease in PCE. This shows that it is important for the performance of the solar cells to retain a strong dipole at the BHJ/MoO_3 interface.

Acknowledgement

Yanting Yin acknowledges the financial support of OSSA from Chinese Government, as well as the support of the Australian National Fabrication Facility (ANFF) and Australian Microscopy & Microanalysis Research Facility (AMMRF) regarding using experimental equipment. X.P., M.R.A. and D.A.L. would like to thank the Australian Research Council for financial support (DP170102467). The authors acknowledge Flinders Microscopy and Microanalysis and the expertise.

Supporting Information

The Supporting Information includes: a) solar cell characterization; b) device fabrication; c) details about XPS fitting; d) UPS of pristine and substrate materials; e) fitting of SVD method; f) weighted shifting method processing the spectra; g) NICISS depth profiling on MoO3 upon Si; h) details of solar cell performance with the calculation of R_s and R_{sh}.

Reference

(1) Xu, X.; Zhang, F.; Zhang, J.; Wang, H.; Zhuo, Z.; Liu, Y.; Wang, J.; Wang, Z.; Xu, Z. High efficient inverted polymer solar cells with different annealing treatment. *Mater. Sci. Eng., C* **2012,** *32* (4), 685-691.
(2) Chambon, S.; Derue, L.; Lahaye, M.; Pavageau, B.; Hirsch, L.; Wantz, G. MoO3 Thickness, Thermal Annealing and Solvent Annealing Effects on Inverted and Direct Polymer Photovoltaic Solar Cells. *Materials* **2012,** *5* (12), 2521-2536.
(3) Lin, R.; Miwa, M.; Wright, M.; Uddin, A. Optimisation of the sol–gel derived ZnO buffer layer for inverted structure bulk heterojunction organic solar cells using a low band gap polymer. *Thin Solid Films* **2014,** *566*, 99-107.
(4) Itoh, E.; Nakagoshi, S. Impedance analysis of the multilayered organic solar cells with and without hole buffer layer. *Jpn. J. Appl. Phys.* **2014,** *53* (4S), 502-503.
(5) Lu, H.-I.; Lu, C.-W.; Lee, Y.-C.; Lin, H.-W.; Lin, L.-Y.; Lin, F.; Chang, J.-H.; Wu, C.-I.; Wong, K.-T. New Molecular Donors with Dithienopyrrole as the Electron-Donating Group for Efficient Small-Molecule Organic Solar Cells. *Chem. Mater.* **2014,** *26* (15), 4361-4367.
(6) Yin, Y.; Sibley, A.; Quinton, J. S.; Lewis, D. A.; Andersson, G. G. Dipole Formation at the MoO3/Conjugated Polymer Interface. *Adv. Funct. Mater.* **2018,** *28* (46), 1802825 -1802835.
(7) Kröger, M.; Hamwi, S.; Meyer, J.; Riedl, T.; Kowalsky, W.; Kahn, A. Role of the deep-lying electronic states of MoO3 in the enhancement of hole-injection in organic thin films. *Appl. Phys. Lett.* **2009,** *95* (12), 123301.
(8) Wang, C.; Irfan, I.; Liu, X.; Gao, Y. Role of molybdenum oxide for organic electronics: Surface analytical studies. *J. Vac. Sci. Technol. B* **2014,** *32* (4), 040801.
(9) Yin, Y.; Lewis, D. A.; Andersson, G. G. The Influence of Moisture on the Energy Level Alignment at the MoO_3/Organic Interfaces. *ACS Appl. Mater. Inter.* **2018,** *10* (50), 44163-44172.
(10) Ishii, H.; Sugiyama, K.; Ito, E.; Seki, K. Energy Level Alignment and Interfacial Electronic Structures at Organic/Metal and Organic/Organic Interfaces. *Adv. Mater.* **1999,** *11* (8), 605-625.
(11) Greiner, M. T.; Helander, M. G.; Tang, W.-M.; Wang, Z.-B.; Qiu, J.; Lu, Z.-H. Universal energy-level alignment of molecules on metal oxides. *Nat. Mater.* **2011,** *11*, 76-81.
(12) Ley, L.; Smets, Y.; Pakes, C. I.; Ristein, J. Calculating the Universal Energy-Level Alignment of Organic Molecules on Metal Oxides. *Adv. Funct. Mater.* **2013,** *23* (7), 794-805.
(13) Braun, S.; Salaneck, W. R.; Fahlman, M. Energy-Level Alignment at Organic/Metal and Organic/Organic Interfaces. *Adv. Mater.* **2009,** *21* (14-15), 1450-1472.
(14) Meyer, J.; Hamwi, S.; Kroger, M.; Kowalsky, W.; Riedl, T.; Kahn, A. Transition metal oxides for organic electronics: energetics, device physics and applications. *Adv. Mater.* **2012,** *24* (40), 5408-5427.
(15) Ng, A.; Liu, X.; To, C. H.; Djurisic, A. B.; Zapien, J. A.; Chan, W. K. Annealing of P3HT:PCBM blend film--the effect on its optical properties. *ACS Appl. Mater. Interfaces* **2013,** *5* (10), 4247-4259.
(16) Lu, Y.; Wang, Y.; Feng, Z.; Ning, Y.; Liu, X.; Lü, Y.; Hou, Y. Temperature-dependent morphology evolution of P3HT:PCBM blend solar cells during annealing processes. *Synth. Met.* **2012,** *162* (23), 2039-2046.
(17) Holmes, N. P.; Marks, M.; Kumar, P.; Kroon, R.; Barr, M. G.; Nicolaidis, N.; Feron, K.; Pivrikas, A.; Fahy, A.; Mendaza, A. D. d. Z.; Kilcoyne, A. L. D.; Müller, C.; Zhou, X.; Andersson, M. R.; Dastoor, P. C.; Belcher, W. J. Nano-pathways: Bridging the divide between water-processable nanoparticulate and bulk heterojunction organic photovoltaics. *Nano Energy* **2016,** *19*, 495-510.
(18) Gartner, S.; Christmann, M.; Sankaran, S.; Rohm, H.; Prinz, E. M.; Penth, F.; Putz, A.;

Tureli, A. E.; Penth, B.; Baumstummler, B.; Colsmann, A. Eco-friendly fabrication of 4% efficient organic solar cells from surfactant-free P3HT:ICBA nanoparticle dispersions. *Adv. Mater.* **2014,** *26* (38), 6653-6660.
(19) Pan, X.; Sharma, A.; Gedefaw, D.; Kroon, R.; Diaz de Zerio, A.; Holmes, N. P.; Kilcoyne, A. L. D.; Barr, M. G.; Fahy, A.; Marks, M.; Zhou, X.; Belcher, W.; Dastoor, P. C.; Andersson, M. R. Environmentally friendly preparation of nanoparticles for organic photovoltaics. *Org. Electron.* **2018,** *59*, 432-440.
(20) Dhanasankar, M.; Purushothaman, K. K.; Muralidharan, G. Effect of temperature of annealing on optical, structural and electrochromic properties of sol–gel dip coated molybdenum oxide films. *Appl. Surf. Sci.* **2011,** *257* (6), 2074-2079.
(21) Pardo, A.; Torres, J. Substrate and annealing temperature effects on the crystallographic and optical properties of MoO3 thin films prepared by laser assisted evaporation. *Thin Solid Films* **2012,** *520* (6), 1709-1717.
(22) Sharma, A.; Pan, X.; Campbell, J. A.; Andersson, M. R.; Lewis, D. A. Unravelling the Thermomechanical Properties of Bulk Heterojunction Blends in Polymer Solar Cells. *Macromolecules* **2017,** *50* (8), 3347-3354.
(23) Abbas, M.; Tekin, N. Balanced charge carrier mobilities in bulk heterojunction organic solar cells. *Appl. Phys. Lett.* **2012,** *101* (7), 073302.
(24) Xiang, D.; Han, C.; Zhang, J.; Chen, W. Gap states assisted MoO3 nanobelt photodetector with wide spectrum response. *Sci Rep* **2014,** *4*, 4891.
(25) Yang, Q.; Yang, D.; Zhao, S.; Huang, Y.; Xu, Z.; Liu, X.; Gong, W.; Fan, X.; Huang, Q.; Xu, X. The improved performance of solution-processed SQ:PC71BM photovoltaic devices via MoO3 as the anode modification layer. *Appl. Surf. Sci.* **2013,** *284*, 849-854.
(26) Kim, J. Y.; Noh, S.; Kwak, J.; Lee, C. Analysis of Annealing Process on P3HT:PCBM-Based Polymer Solar Cells Using Optical and Impedance Spectroscopy. *J. Nanosci. Nanotechnol* **2013,** *13* (5), 3360-3364.
(27) Abramavicius, V.; Amarasinghe Vithanage, D.; Devizis, A.; Infahsaeng, Y.; Bruno, A.; Foster, S.; Keivanidis, P. E.; Abramavicius, D.; Nelson, J.; Yartsev, A.; Sundstrom, V.; Gulbinas, V. Carrier motion in as-spun and annealed P3HT:PCBM blends revealed by ultrafast optical electric field probing and Monte Carlo simulations. *Phys. Chem. Chem. Phys.* **2014,** *16* (6), 2686-2692.
(28) Chang, W.-C.; Qi, X.; Kuo, J.-C.; Lee, S.-c.; Ng, S.-K.; Chen, D. Post-deposition annealing control of phase and texture for the sputtered MoO3 films. *CrystEngComm* **2011,** *13* (16), 5125–5132.
(29) Battaglia, C.; Yin, X.; Zheng, M.; Sharp, I. D.; Chen, T.; McDonnell, S.; Azcatl, A.; Carraro, C.; Ma, B.; Maboudian, R.; Wallace, R. M.; Javey, A. Hole selective MoOx contact for silicon solar cells. *Nano Lett.* **2014,** *14* (2), 967-971.
(30) Dasgupta, B.; Goh, W. P.; Ooi, Z. E.; Wong, L. M.; Jiang, C. Y.; Ren, Y.; Tok, E. S.; Pan, J.; Zhang, J.; Chiam, S. Y. Enhanced Extraction Rates through Gap States of Molybdenum Oxide Anode Buffer. *J. Phys. Chem. C* **2013,** *117* (18), 9206-9211.
(31) Hermerschmidt, F.; Savva, A.; Georgiou, E.; Tuladhar, S. M.; Durrant, J. R.; McCulloch, I.; Bradley, D. D. C.; Brabec, C. J.; Nelson, J.; Choulis, S. A. Influence of the Hole Transporting Layer on the Thermal Stability of Inverted Organic Photovoltaics Using Accelerated-Heat Lifetime Protocols. *ACS Appl. Mater. Inter.* **2017,** *9* (16), 14136-14144.
(32) Greiner, M. T.; Chai, L.; Helander, M. G.; Tang, W.-M.; Lu, Z.-H. Transition Metal Oxide Work Functions: The Influence of Cation Oxidation State and Oxygen Vacancies. *Adv. Funct. Mater.* **2012,** *22* (21), 4557-4568.
(33) Song, Z.; Cai, T.; Chang, Z.; Liu, G.; Rodriguez, J. A.; Hrbek, J. Molecular Level Study of the Formation and the Spread of MoO3 on Au (111) by Scanning Tunneling Microscopy and X-ray Photoelectron Spectroscopy. *J. Am. Chem. Soc.* **2003,** *125* (26), 8059-8066.

(34) Vasilopoulou, M.; Palilis, L. C.; Georgiadou, D. G.; Douvas, A. M.; Argitis, P.; Kennou, S.; Sygellou, L.; Papadimitropoulos, G.; Kostis, I.; Stathopoulos, N. A.; Davazoglou, D. Reduction of Tungsten Oxide: A Path Towards Dual Functionality Utilization for Efficient Anode and Cathode Interfacial Layers in Organic Light-Emitting Diodes. *Adv. Funct. Mater.* **2011,** *21* (8), 1489-1497.
(35) Volgmann, K.; Voigts, F.; Maus-Friedrichs, W. The interaction of H2O molecules with iron films studied with MIES, UPS and XPS. *Surf. Sci.* **2012,** *606*, 858-864.
(36) Dahle, S.; Meuthen, J.; Viöl, W.; Maus-Friedrichs, W. Adsorption of silver on glucose studied with MIES, UPS, XPS and AFM. *Appl. Surf. Sci.* **2013,** *284*, 514-522.
(37) Berlich, A.; Liu, Y.-C.; Morgner, H. Growth of nickel nanoparticles on NiO/Ni(001): Evidence of adsorbed oxygen on metal particles by metastable induced electron spectroscopy (MIES). *Surf. Sci.* **2008,** *602* (24), 3737-3744.
(38) Berlich, A.; Liu, Y. C.; Morgner, H. Evaporation of Ni and Carbon Containing Species onto NiO/Ni as Case Study for Metal Support Catalysts Investigated by Metastable Induced Electron Spectroscopy (MIES). *Radiat. Phys. Chem.* **2005,** *74* (3-4), 201-209.
(39) Andersson, G.; Morgner, H. Impact collision ion scattering spectroscopy (ICISS) and neutral impact collision ion scattering spectroscopy (NICISS) at surfaces of organic liquids. *Surf. Sci.* **1997,** *405*, 138-151.
(40) Ridings, C.; Andersson, G. G. Deconvolution of NICISS profiles involving elements of similar masses. *Nucl. Instrum. Methods. Phys. Res. B* **2014,** *340*, 63-66.
(41) Andersson, G.; Morgner, H.; Schulze, K. D. Surface properties of electrolyte solutions studied with ion beam analysis. *Nucl. Instrum. Methods. Phys. Res. B* **2002,** *190* (1-4), 222-225.
(42) Andersson, G. Energy-loss straggling of helium projectiles at low kinetic energies. *Phys. Rev. A* **2007,** *75* (3), 032901.
(43) Sharma, A.; Berger, R.; Lewis, D. A.; Andersson, G. G. Invisible high workfunction materials on heterogeneous surfaces. *Appl. Surf. Sci.* **2015,** *327*, 22-26.
(44) Oberbrodhage, J. Determination of a solute electron energy spectrum not accessible experimentally by means of Singular Value Decomposition. *J. Electron. Spectrosc. Relat. Phenom.* **2000,** *170*, 231–238.
(45) Chambers, B. A.; Neumann, C.; Turchanin, A.; Gibson, C. T.; Andersson, G. G. The direct measurement of the electronic density of states of graphene using metastable induced electron spectroscopy. *2D Mater.* **2017,** *4* (2), 025068.
(46) Baek, W.-H.; Yang, H.; Yoon, T.-S.; Kang, C. J.; Lee, H. H.; Kim, Y.-S. Effect of P3HT:PCBM concentration in solvent on performances of organic solar cells. *Sol. Energy Mater. Sol. Cells* **2009,** *93* (8), 1263-1267.
(47) Kumar, P.; Singh, M.; Sharma, R. K.; Reddy, G. B. Reaction mechanism of core–shell MoO2/MoS2nanoflakes via plasma-assisted sulfurization of MoO3. *Mater. Res. Express.* **2016,** *3* (5), 055021.
(48) Bai, S.; Chen, C.; Tian, Y.; Chen, S.; Luo, R.; Li, D.; Chen, A.; Liu, C. C. Facile synthesis of α-MoO3 nanorods with high sensitivity to CO and intrinsic sensing performance. *Mater. Res. Bull.* **2015,** *64*, 252-256.
(49) Andreoli, E.; Barron, A. CO2 Adsorption by para-Nitroaniline Sulfuric Acid-Derived Porous Carbon Foam. *C.* **2016,** *2* (4), 25-34.
(50) Zhu, H.; Li, K.; Chen, M.; Cao, H.; Wang, F. A Novel Metal–Organic Framework Route to Embed Co Nanoparticles into Multi-Walled Carbon Nanotubes for Effective Oxygen Reduction in Alkaline Media. *Catal.* **2017,** *7* (12), 364-377.
(51) Yuan, N.; Li, J.; Lin, C. Valence reduction process from sol-gel V2O5 to VO2 thin films. *Appl. Surf. Sci.* **2002,** *191*, 176-180.
(52) Ahmadpour, M.; Fernandes Cauduro, A. L.; Méthivier, C.; Kunert, B.; Labanti, C.; Resel,

R.; Turkovic, V.; Rubahn, H.-G.; Witkowski, N.; Schmid, A. K.; Madsen, M. Crystalline Molybdenum Oxide Layers as Efficient and Stable Hole Contacts in Organic Photovoltaic Devices. *ACS Appl. Energy Mater.* **2019,** *2* (1), 420-427.
(53) Ohkita, H.; Nomura, Y.; Tsuchida, A.; Yamamoto, M. Direct observation of the carbazole hole trap in polymer solid films by the charge-resonance band. *Chem. Phys. Lett.* **1996,** *263*, 602-606.
(54) Zhang, M.; Irfan; Ding, H.; Gao, Y.; Tang, C. W. Organic Schottky barrier photovoltaic cells based on MoOx/C60. *Appl. Phys. Lett.* **2010,** *96* (18), 183301.
(55) Bao, Q.; Sandberg, O.; Dagnelund, D.; Sandén, S.; Braun, S.; Aarnio, H.; Liu, X.; Chen, W. M.; Österbacka, R.; Fahlman, M. Trap-Assisted Recombination via Integer Charge Transfer States in Organic Bulk Heterojunction Photovoltaics. *Adv. Funct. Mater.* **2014,** *24* (40), 6309-6316.
(56) Howard, J. B.; Noh, S.; Beier, A. E.; Thompson, B. C. Fine Tuning Surface Energy of Poly(3-hexylthiophene) by Heteroatom Modification of the Alkyl Side Chains. *ACS Macro Lett.* **2015,** *4* (7), 725-730.
(57) Chen, L.; Xu, Z.; Hong, Z.; Yang, Y. Interface investigation and engineering – achieving high performance polymer photovoltaic devices. *J. Mater. Chem.* **2010,** *20* (13), 2575–2598.
(58) Papakondylis, A.; Sautet, P. Ab Initio Study of the Structure of the α-MoO3 Solid and Study of the Adsorption of H2O and CO Molecules on Its (100) Surface. *J. Phys. Chem. B* **1996,** *100* (25), 10681–10688.
(59) Hayashi, N.; Ishii, H.; Ouchi, Y.; Seki, K. Examination of band bending at buckminsterfullerene (C60)/metal interfaces by the Kelvin probe method. *J. Appl. Phys.* **2002,** *92* (7), 3784-3793.
(60) Irfan; Zhang, M.; Ding, H.; Tang, C. W.; Gao, Y. Strong interface p-doping and band bending in C60 on MoOx. *Org. Electron.* **2011,** *12* (9), 1588-1593.
(61) Battaglia, C.; de Nicolás, S. M.; De Wolf, S.; Yin, X.; Zheng, M.; Ballif, C.; Javey, A. Silicon heterojunction solar cell with passivated hole selective MoOx contact. *Appl. Phys. Lett.* **2014,** *104* (11), 113902.

Table of Content

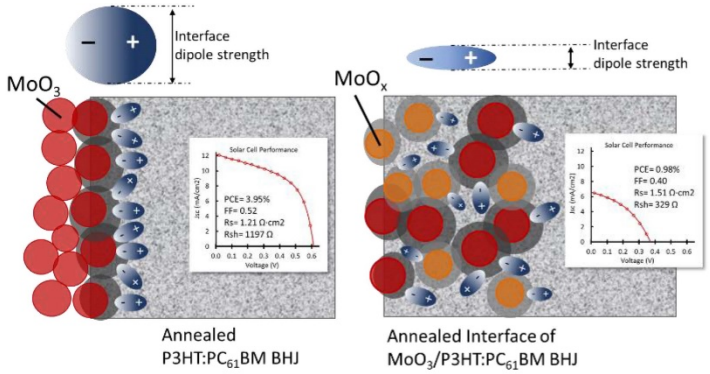

Annealing of the MoO_3/BHJ interface leads to diffusion of the MoO_3 into the BHJ, reduces the interface dipole and the efficiency of the photovoltaic device. Pre-annealing of the BHJ before the deposition of MoO_3 does not lead to diffusion, retains the strong interface dipole and results in a higher efficiency of the photovoltaic device.

Supporting Information

Mechanism of Organic Solar Cell Performance Degradation upon Thermal Annealing of MoO_x

Yanting Yin[1,2], Xun Pan[1], Mats R. Andersson[1], David A. Lewis[1] and Gunther G. Andersson*[1,2]

1 Flinders Institute for Nanoscale Science and Technology, Flinders University, Adelaide SA 5042, Australia

2 Flinders Microscopy and Microanalysis, College of Science and Engineering, Flinders University, Adelaide, SA 5042, Australia

** Gunther.Andersson@flinders.edu.au*

Solar simulator and J-V characterization: J-V properties of solar cells were measured in air by an Oriel solar simulator fitted with a 150 W Xenon lamp (Newport), filtered to give an irradiation of 100 mW/cm^2 at AM1.5 and calibrated using a silicon reference cell with NIST traceable certification. The characteristics of devices were measured through a Keithley 2400 source meter unit. Dark J-V curve was also recorded for characterizing the diode characteristics and resistance differential[1], from which the series resistance (R_s) and shunt resistance (R_{sh}) were obtained.

Device fabrication: To characterize the P3HT:$PC_{61}BM$ based solar cell performance, inverted organic solar cells with the structure ITO/ZnO/BHJ/MoO_3/Ag were fabricated. ITO-coated glass substrates were first cleaned by soaking in a 5% detergent solution (Pyroneg from

Johnson Diversey) at 90 °C for 20 minute and then rinsing in deionized (DI) water, before sonicating in DI water, acetone and isopropanol for 10 min each. Substrates were then cleaned in UV-ozone for 20 minute immediately before spin coating the ZnO layer. ZnO sol-gel[2] on the cleaned ITO substrate was heated at 280 °C for 10 minute in air to yield an approximate 25 nm thick film. The P3HT:$PC_{61}BM$ (1:1) BHJ layer was deposited from 30 mg/mL chlorobenzene: *o*-DCB (7:3 volume ratio) solution onto ZnO/ITO coated substrates using the spin-coating condition of 2200 rpm for 1 min. The pre-annealed devices are referred to the devices with only P3HT:$PC_{61}BM$ BHJ layer thermally annealed at 170 °C for 10 min in a N_2 ambient glove box. Then 12nm MoO_3 layer was thermally evaporated on top of the active layer. In the case of devices treated with post-annealing (BHJ non-annealed) and 2-stage annealing (BHJ annealed), incomplete devices coated with MoO_3 were thermally annealed at 170 °C for 10 min in the glove box. Finally the Ag electrode (80 nm) was deposited by thermally evaporating through a shadow mask, which defined the active area to be 0.1 cm^2.

Analysis of the XP spectra

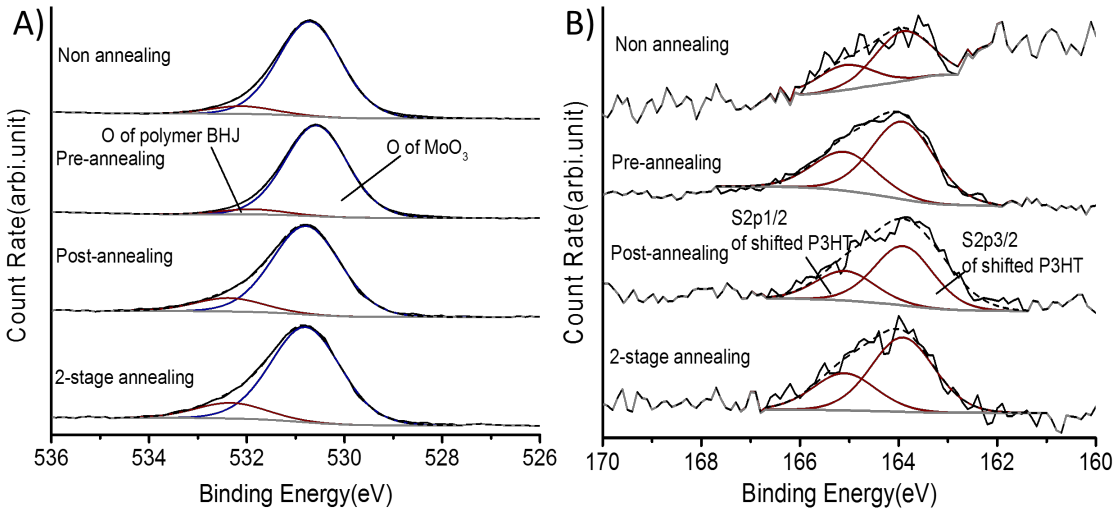

Figure S 1. Fitted XP spectra of O A) and S B) of the samples

The high resolution XPS scans of O and S are shown in Figure S1. O1s shows two individual contributions with one peak at 530.6 ± 0.15 eV assigned to MoO_3 [3] and a second peak at 532.1~532.6 eV related to polymer BHJ[4]. The S2p contribution shown in Figure S1 (B) can be fitted with a single doublet S $2p_{3/2}$ contribution. The S is from the thiophene ring of P3HT forming one component of the polymer BHJ. The binding energy is 163.9 ± 0.15eV for $S2p_{3/2}$.

Data Analysis of UPS with IPES

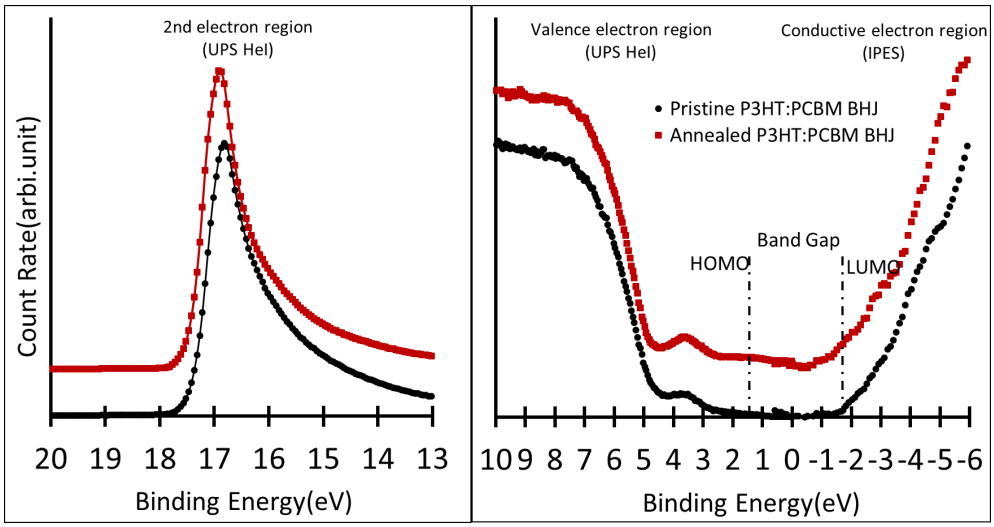

Figure S 2. UP and IPE spectra of a pristine polymer BHJ sample before and after annealing at 170°C for 10min, no obvious change upon the structure of energy states has been observed

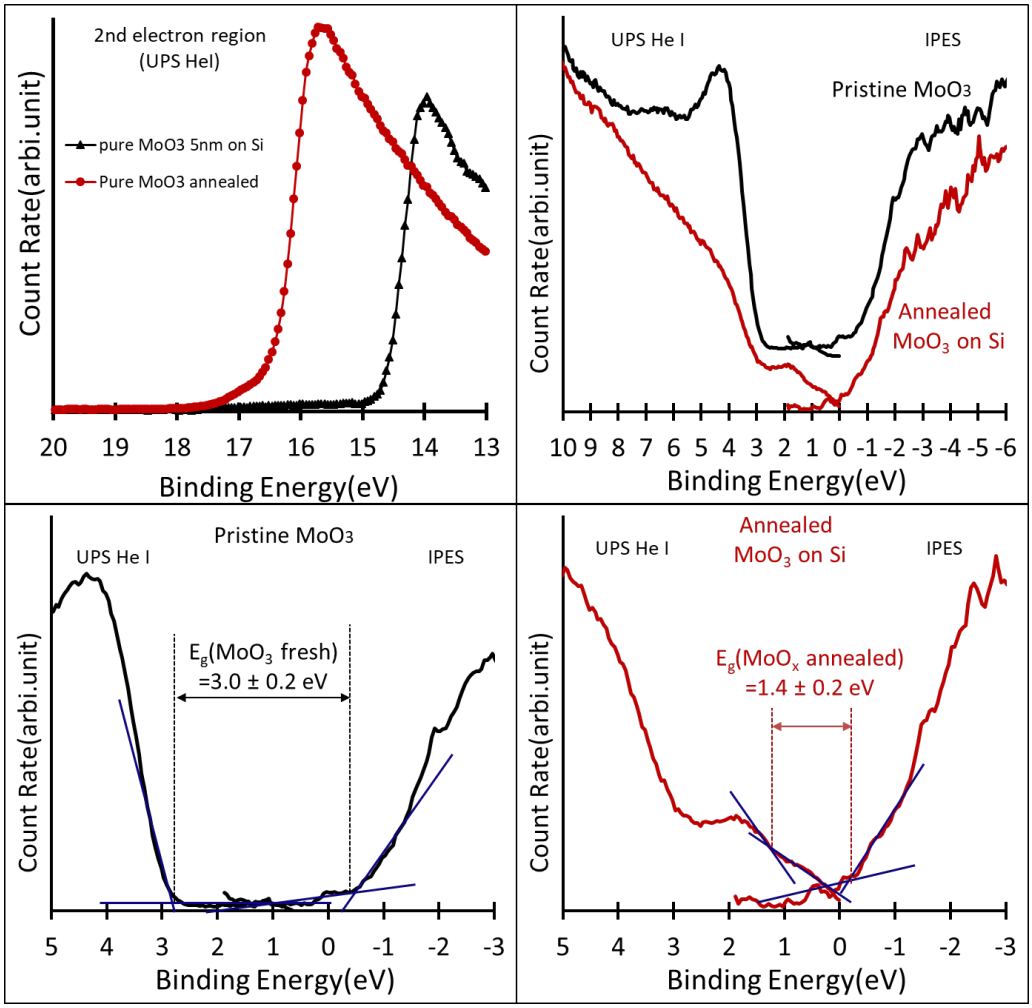

Figure S 3. UP and IPE spectra of a 5nm MoO_3 layer on Si as deposited (pure) and after annealing at 170°C for 10min. Figures below illustrate the extraction of band gap of fresh MoO_3 and annealed MoO_x from the edge of valence and conduction electron peaks

The valence electron spectra (UPS) and conduction electron spectra (IPES) of a 6nm MoO_3/Si sample are shown in Figure S3. Vacuum annealing has been applied to the sample. The band gap o MoO_3 found here is around 3.2eV and in agreement with literature values[5]. The band gap of MoO_3 does not change upon annealing. However, the contribution at the valence band edge at 3 eV of the pristine MoO_3 decreases and new states can be found within the band gap. Appearance of new states close to Fermi level indicates the formation of more metallic states which usually leads to a higher conductivity [6-9]. It is important to point out that before annealing

the 6nm MoO_3 forms a closed layer on Si. Such MoO_3 layer can change morphology upon annealing and the formation aggregates and thus a layer with inhomogeneous thickness [10]. In case the MoO_3 turns into aggregates, the valence electron spectrum of the annealed MoO_3 has to be considered as a linear combination of SiO_2 and MoO_3. However, the onset of the valence electron contribution of SiO_2 is at a much higher binding energy than for MoO_3 thus in practise the spectra shown in Figure S3 are showing to a very large degree only MoO_3.

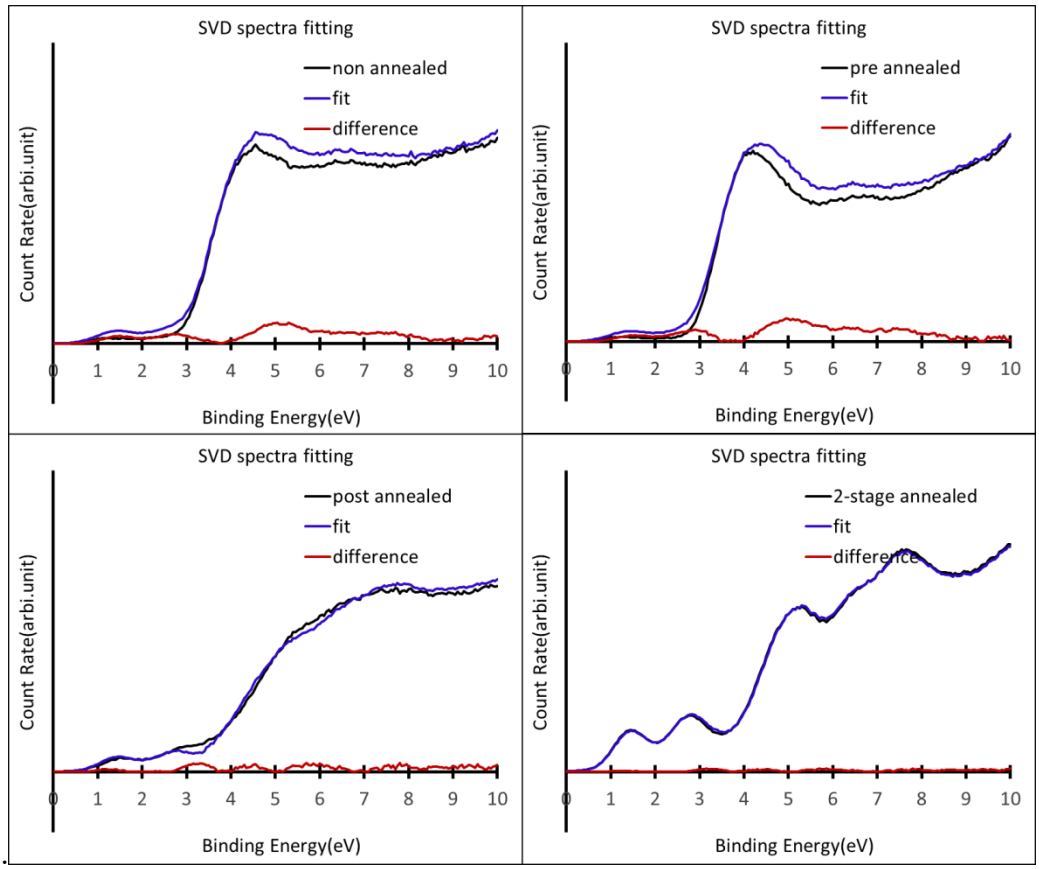

Figure S 4. The fitting of UP spectra using SV decomposition method

The fitting of UP spectra is shown in Figure S4 of all samples. The SVD algorithm has been performed and reference spectra were identified. The fitting is reasonable with a minor residue which can be seen.

Oppositely a large fraction BHJ with minor energy shift can be seen by post-annealing the MoO_3/BHJ sample however the dipole strength can be dramatically deteriorated. The mean energy shift (ΔE_{mean}) being illustrated as inset in Figure 5 D can be carried out by following the Equation S1. The calculation of ΔE_{mean} has been adopted in our previous report with a similar form[11].

$$\Delta E_{mean} = \frac{(j_a \cdot \Delta E_a + j_b \cdot \Delta E_b)}{j_a + j_b} \qquad \text{Equation S1}$$

Here from SVD ΔE indicates the energy shift found for reference spectra, ΔE_a is assigned to pristine BHJ, which shows zero energy shift. ΔE_b is in relevance to BHJ with an energy shift of approximately 2.0eV to lower binding energy. j_a and j_b thus represents the individual weighting factors. The ΔE_{mean} is thus calculated as 1.7eV for pre-annealed sample, which declines from pristine sample by 0.1eV, and for sample post-annealing and 2-stage annealing it levels at 0.5eV and 0.2eV. The decrease in dipole strength can be due to either the change in local strength of the dipole at the MoO_3/BHJ interface or a decrease in the intensity of the BHJ component shifted on the energy scale because of a dipole related to the diffusion of the MoO_3 to a deeper layer in the BHJ. Only in case the BHJ has been annealed before depositing the MoO_3 (pre-annealed) the diffusion of MoO_3 into the BHJ is stopped and the strong dipole at the MoO_3/BHJ interface retained.

Further Investigation using Weighted-Shifting Decomposition Method

The weighted shifting procedure of fitting has been developed [11-12]. The algorithm advantages at identifying step-wise energy shift of BHJ spectra thus determine the dipole energy and is

applied on UP spectra. All reference spectra from SVD are used for fitting the spectra. The algorithm is described as Equation S2-S3

$$S^i_{meas} = \sum_{j=0}^{n} a^i_j \times S_{BHJ}\left(E + j \cdot \Delta E\right) + b \cdot S_{MoO_3} + c \cdot S_{a-MoO_x} \quad \text{Equation S2}$$
$$\text{with} \quad \sum_j a^i_j + b + c = 1$$

$$\Delta E^i_{mean} = \sum_{j=0}^{n} a^i_j \cdot j \cdot \Delta E \quad \text{Equation S3}$$

S_{BHJ} : the spectrum of the BHJ layer (Ref. B)

S_{MoO3} : the spectrum of MoO_3 (Ref. A)

$S_{a\text{-}MoOx}$: the spectrum of annealed MoO_x (Ref. D), which is identified from SVD

ΔE : an energy increment

$j \cdot \Delta E$: an integer multiple of the energy increment for which S_{BHJ} is shifted in applying Equation S2

The sum of the weighting factors has to be unity within experimental uncertainty, but an error of about 0.1 is acceptable.

The reference spectra found in SVD have been further preceded upon the measured spectra valence electron region with Equation S2 for quantifying the distribution of energy shift. The distribution of energy shift of BHJ and the correspondent weighting factor of BHJ are shown in Figure S5 (A). While the mean energy shift calculated using Equation S3 is shown as the inset. The weighting factor of MoO_3 and annealed MoO_x is shown in Figure S5 (B)

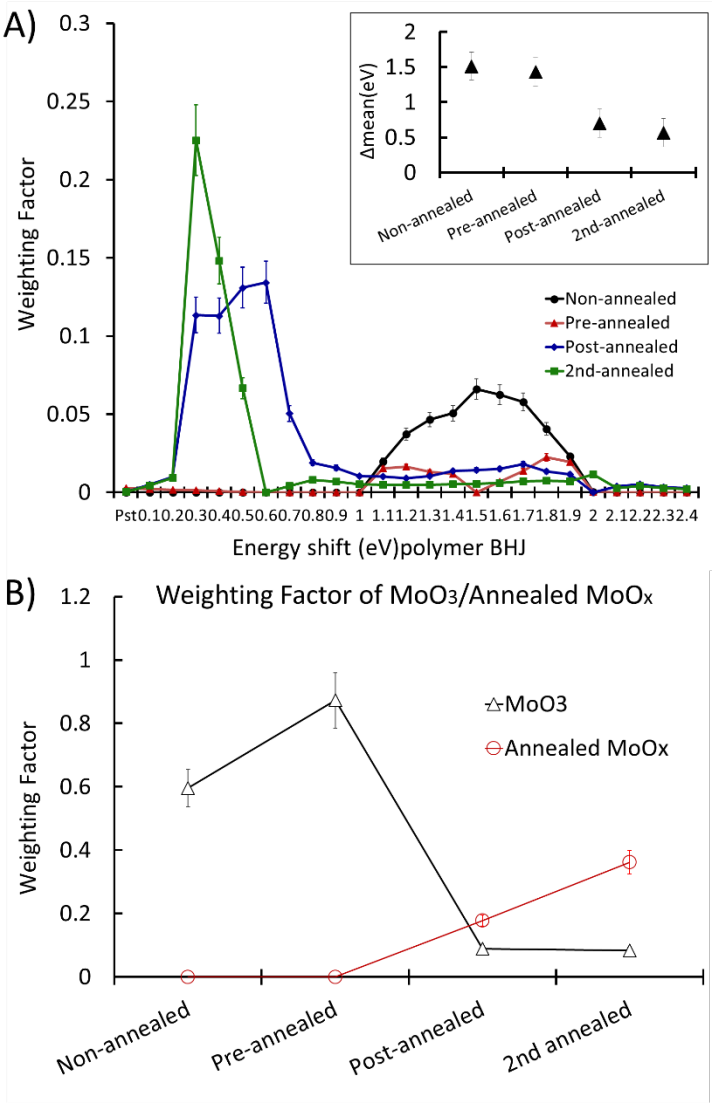

Figure S 5. (A) The distribution of energy shift of BHJ under different annealing conditions, the inset in the figure shows the mean energy shift; (B) The weighting factors of MoO_3 and annealed MoO_x

The distribution of energy shift of BHJ was found for the samples. It is evident that the distribution shifts to a lower binding energy region for post-annealed and two-stage annealed samples, indicating the dipole at the interface is lessened. The mean energy shift (ΔE^i_{mean}) levels at about 1.5eV for non-annealed and pre-annealed samples. For post-annealed sample, the ΔE^i_{mean} noticeably decreases to 0.4~0.6eV. The decrease is in agreement with the ΔE^i_{mean}

from SVD in main content. The change of dipole strength which causes the decrease of energy shift of BHJ for annealed samples can be certainly validated with two different decomposition procedures.

NICISS Result of Thermal-treated 4nm MoO_3/BHJ sample

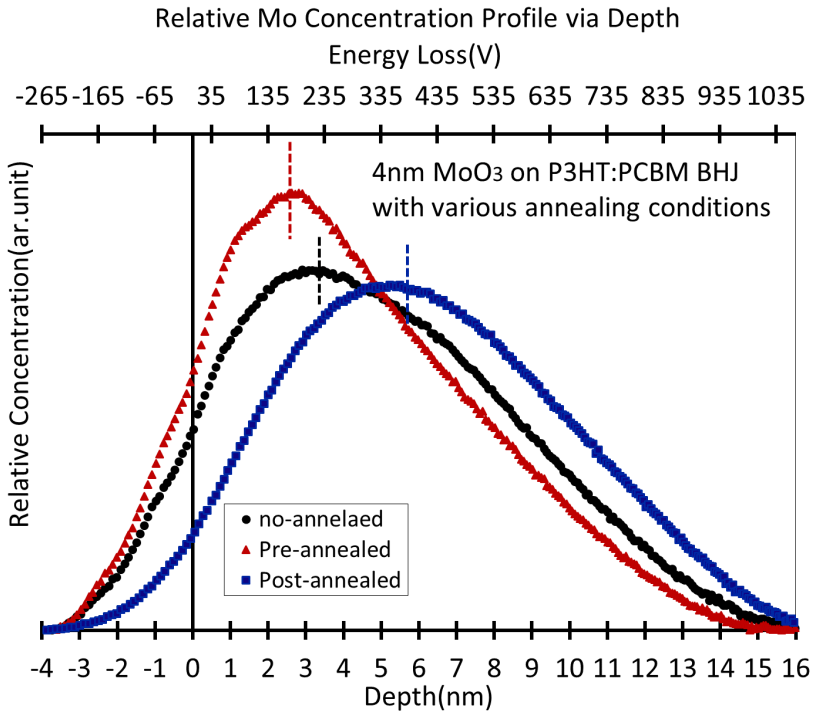

Figure S 6. NICISS result shows the distribution of MoO_3 of 4nm MoO_3/BHJ samples under various annealing treatments, the shadow part indicates the surface and bulk of polymer BHJ

In Figure S6, the concentration depth profile of Mo at the BHJ/MoO_3 interface is shown for 4 nm MoO_3. a shift of the peak to the inner side of the BHJ substrate can be found with post-annealed proceeded. The Mo concentration of the post-annealing sample peaks at ~6 nm whereas the maxima of Mo concentration of the non-annealed sample is found at ~4nm and that of the pre-annealed sample at ~3nm. This finding is similar to that of the 1.5nm MoO_3/BHJ samples.

Solar Cell Device Performance

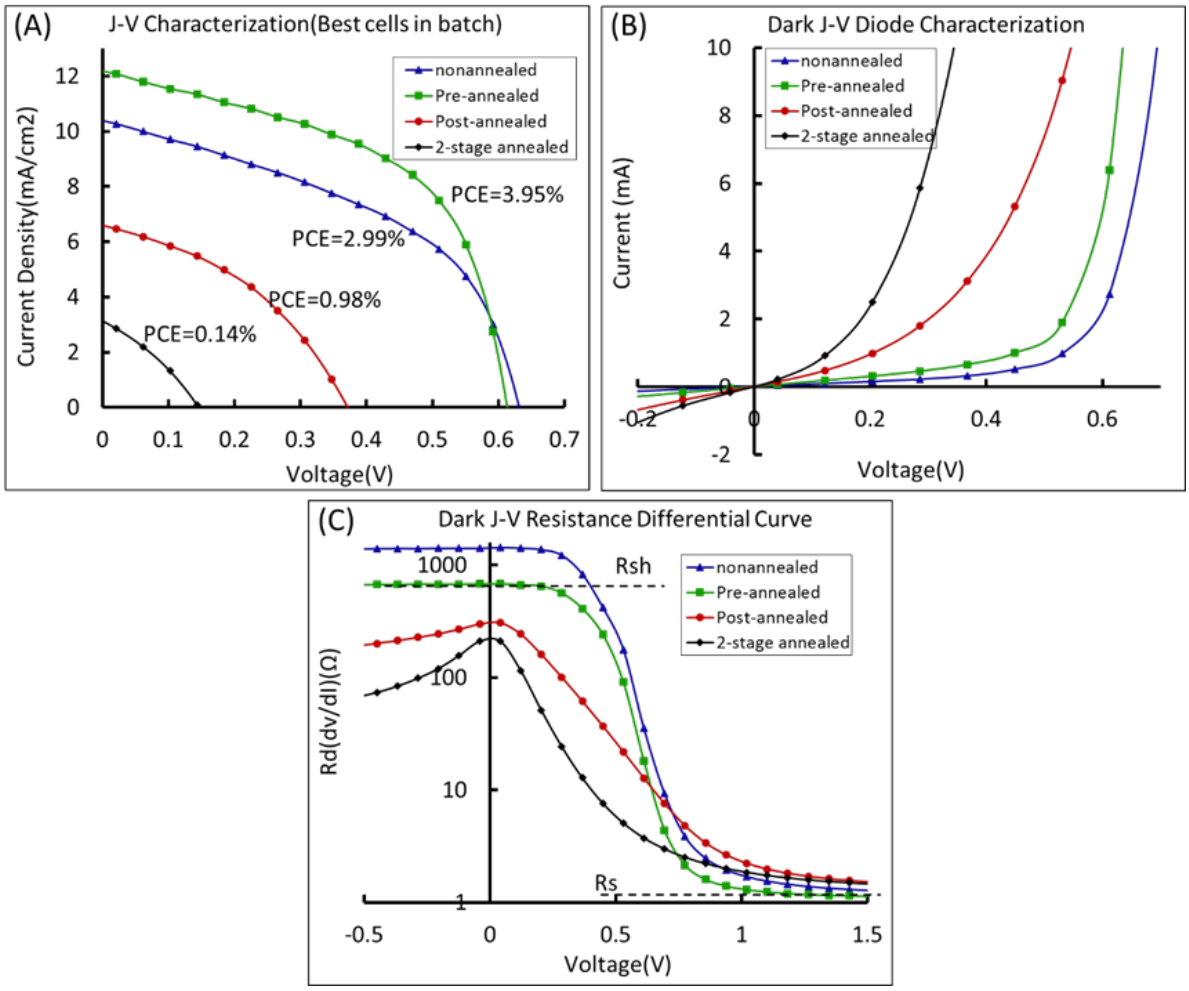

Figure S 7. (A) J-V curve of the solar cells under AM1.5 for different annealing conditions, only the solar cells with highest performance are shown; (B) Dark J-V curve of the same solar cells indicating the diode characteristics; (C) Resistance differential via voltage of the correspondent solar cells is shown. The R_s and R_{sh} were extrapolated from the curve off-sets, which is described in experimental section. Note that the Rd in (C) is shown with a logarithmic scale for the resistance.

Annealing condition	**PCE (%) (±0.06)**	**Voc(V) (±0.02)**	**Jsc (mA/cm2) (±0.35)**	**Fill Factor (%) (±1.15)**

Non-annealed sample	2.78	0.65	9.97	43.00
	2.99	0.63	10.39	46.00
	2.88	0.63	9.94	46.00
	2.67	0.63	9.62	44.00
	2.85	0.63	9.99	45.00
	2.95	0.63	10.21	46.00
Pre-annealing upon BHJ before MoO_3 deposition	3.84	0.63	11.90	51.00
	3.64	0.62	11.83	49.00
	3.66	0.63	11.33	52.00
	3.95	0.63	12.17	52.00
	3.60	0.63	11.07	52.00
	3.59	0.62	10.37	56.00
Post-annealing after MoO_3 deposition	0.83	0.36	5.77	40.00
	0.85	0.34	6.50	39.00
	0.82	0.33	6.40	39.00
	0.98	0.37	6.60	40.00
	0.96	0.37	6.40	40.00
	0.95	0.35	6.81	40.00
2-stage annealing before and after MoO_3 deposition	0.11	0.14	2.60	30.00
	0.14	0.15	3.13	30.00
	0.13	0.15	3.08	30.00
	0.12	0.13	2.87	31.00

	0.10	0.13	2.65	31.00
	0.10	0.12	2.56	31.00

Table S1. Characterization of the polymer based solar cells with different annealing process for all 6 solar cells of each batch.

Reference

(1) Viktor V. Brus; Christopher M. Proctor; Niva A. Ran; Nguyen, T.-Q. Capacitance Spectroscopy for Quantifying Recombination Losses in Nonfullerene Small-Molecule Bulk Heterojunction Solar Cells. *Adv. Energy Mater* **2016,** *6* (1502250), 1-8.
(2) Yanming Sun; Jung Hwa Seo; Christopher J. Takacs ; Jason Seifter; Heeger, A. J. Inverted Polymer Solar Cells Integrated with a Low‐Temperature‐Annealed Sol‐Gel‐Derived ZnO Film as an Electron Transport Layer. *Adv. Mater.* **2011,** *23* (14), 1679-1683.
(3) Imran, S.; Muhammad, S.; Dae, J. K. MoO3 and Cu0.33MoO3 nanorods for unprecedented UV/Visible light photocatalysis. *Chem. Commun.* **2010,** (24).
(4) Maibach, J.; Mankel, E.; Mayer, T.; Jaegermann, W. The band energy diagram of PCBM–DH6T bulk heterojunction solar cells: synchrotron-induced photoelectron spectroscopy on solution processed DH6T:PCBM blends and in situ prepared PCBM/DH6T interfaces. *J. Mater. Chem. C* **2013,** *1* (45), 7635.
(5) Kröger, M.; Hamwi, S.; Meyer, J.; Riedl, T.; Kowalsky, W.; Kahn, A. Role of the deep-lying electronic states of MoO3 in the enhancement of hole-injection in organic thin films. *Appl. Phys. Lett.* **2009,** *95* (12), 123301.
(6) Vasilopoulou, M.; Palilis, L. C.; Georgiadou, D. G.; Douvas, A. M.; Argitis, P.; Kennou, S.; Sygellou, L.; Papadimitropoulos, G.; Kostis, I.; Stathopoulos, N. A.; Davazoglou, D. Reduction of Tungsten Oxide: A Path Towards Dual Functionality Utilization for Efficient Anode and Cathode Interfacial Layers in Organic Light-Emitting Diodes. *Adv. Funct. Mater.* **2011,** *21* (8), 1489-1497.
(7) Yuan, N.; Li, J.; Lin, C. Valence reduction process from sol-gel V2O5 to VO2 thin films. *Appl. Surf. Sci.* **2002,** *191*, 176-180.
(8) Dang, J.; Zhang, G.-H.; Chou, K.-C. Phase Transitions and Morphology Evolutions during Hydrogen Reduction of MoO3 to MoO2. *High Temp. Mater. Processes* **2014,** *33* (4).
(9) Greiner, M. T.; Chai, L.; Helander, M. G.; Tang, W.-M.; Lu, Z.-H. Transition Metal Oxide Work Functions: The Influence of Cation Oxidation State and Oxygen Vacancies. *Adv. Funct. Mater.* **2012,** *22* (21), 4557-4568.
(10) Ma, W.; Zhang, C.; Liu, C.; Nan, X.; Fu, H.; Cao, G. Impacts of Surface Energy on Lithium Ion Intercalation Properties of V2O5. *ACS Appl. Mater. Interfaces* **2016,** *8* (30), 19542–19549.
(11) Yin, Y.; Sibley, A.; Quinton, J. S.; Lewis, D. A.; Andersson, G. G. Dipole Formation at the MoO3/Conjugated Polymer Interface. *Adv. Funct. Mater.* **2018,** *28* (46), 1802825 - 1802835.
(12) Berlich, A.; Liu, Y.-C.; Morgner, H. Growth of nickel nanoparticles on NiO/Ni(001): Evidence of adsorbed oxygen on metal particles by metastable induced electron spectroscopy (MIES). *Surf. Sci.* **2008,** *602* (24), 3737-3744.